

Atherosclerotic tissue characterization *in vivo* by optical coherence tomography attenuation imaging

Gijs van Soest

Thadé Goderie

Evelyn Regar

Erasmus Medical Center
Thorax Center
PO Box 2040
Rotterdam 3000CA
The Netherlands

Senada Koljenović

Geert L. J. H. van Leenders

Erasmus Medical Center
Department of Pathology
PO Box 2040
Rotterdam 3000CA
The Netherlands

Nieves Gonzalo

Sander van Noorden

Takayuki Okamura

Erasmus Medical Center
Thorax Center
PO Box 2040
Rotterdam 3000CA
The Netherlands

Brett E. Bouma

Massachusetts General Hospital
Wellman Center for Photomedicine
40 Blossom Street
Boston, Massachusetts 02114
and
Department of Dermatology
Harvard Medical School
Boston Massachusetts
and
Harvard-Massachusetts Institute of Technology
Division of Health Sciences and Technology
Cambridge, Massachusetts 02139

Guillermo J. Tearney

Massachusetts General Hospital
Wellman Center for Photomedicine
40 Blossom Street
Boston, Massachusetts 02114
and
Harvard-Massachusetts Institute of Technology
Division of Health Sciences and Technology
Cambridge, Massachusetts
and
Harvard Medical School
Department of Pathology
Boston, Massachusetts 02114

J. Wolter Oosterhuis

Erasmus Medical Center
Department of Pathology
PO Box 2040
Rotterdam 3000CA
The Netherlands

Patrick W. Serruys

Erasmus Medical Center
Thorax Center
PO Box 2040
Rotterdam 3000CA
The Netherlands

Anton F. W. van der Steen

Erasmus Medical Center
Thorax Center
PO Box 2040
Rotterdam 3000CA
The Netherlands
and
Institute of the Netherlands
Interuniversity Cardiology
Utrecht, The Netherlands

Abstract. Optical coherence tomography (OCT) is rapidly becoming the method of choice for assessing arterial wall pathology *in vivo*. Atherosclerotic plaques can be diagnosed with high accuracy, including measurement of the thickness of fibrous caps, enabling an assessment of the risk of rupture. While the OCT image presents morphological information in highly resolved detail, it relies on interpretation of the images by trained readers for the identification of vessel wall components and tissue type. We present a framework to enable systematic and automatic classification of atherosclerotic plaque constituents, based on the optical attenuation coefficient μ_t of the tissue. OCT images of 65 coronary artery segments *in vitro*, obtained from 14 vessels harvested at autopsy, are analyzed and correlated with histology. Vessel wall components can be distinguished based on their optical properties: necrotic core and macrophage infiltration exhibit strong attenuation, $\mu_t \geq 10 \text{ mm}^{-1}$, while calcific and fibrous tissue have a lower $\mu_t \approx 2-5 \text{ mm}^{-1}$. The algorithm is successfully applied to OCT patient data, demonstrating that the analysis can be used in a clinical setting and assist diagnostics of vessel wall pathology. © 2010 Society of Photo-Optical Instrumentation Engineers. [DOI: 10.1117/1.3280271]

Keywords: biomedical optics; attenuation; endoscopy; tissues; medicine; medical imaging.

Paper 09170SSR received Apr. 29, 2009; revised manuscript received Aug. 10, 2009; accepted for publication Aug. 18, 2009; published online Jan. 15, 2010.

1 Introduction

1.1 Background

It is generally accepted that the majority of acute coronary events is precipitated by the rupture of a vulnerable atherosclerotic plaque in the coronary system, and subsequent thrombogenesis.¹⁻³ The thin-cap fibroatheroma is currently hypothesized to be the most likely class of arterial wall pathology to constitute a vulnerable plaque.^{4,5} The key to plaque

Address all correspondence to: Gijs van Soest, PhD, Erasmus MC, Thorax Center, PO Box 2040, Rotterdam 3000CA, The Netherlands. Tel: 31-10-7044638; Fax: 31-10-7044720; E-mail: g.vansoest@erasmusmc.nl

vulnerability is still elusive,⁶ even though recent technological advances in intravascular imaging technology have enabled the collection of a wealth of data on unstable atherosclerosis in all its stages of development,⁷ both in clinical and in *ex vivo* settings. It appears very likely that combined information on physiological, anatomical, chemical, and mechanical parameters^{8–10} is required for a reliable assessment of the proneness of a specific lesion to rupture. Some of these parameters may be accessible through intravascular imaging methods.^{11–19} In addition, plaque type and morphology prior to intervention influence the long-term procedural outcome significantly.²⁰ Among the parameters that influence plaque vulnerability are the thickness of the fibrous cap overlying the necrotic core, inflammation, intraplaque hemorrhage, and composition.^{9,21} Data on plaque composition and stability can complement the image, and can aid decisions regarding whether a particular section of coronary artery should be treated and how.

The advent of optical coherence tomography (OCT) for cardiovascular applications has boosted the resolving power of intravascular imaging to a level where imaging the thin cap of a vulnerable plaque is possible.²² Insight into the physiology of a plaque is complementary to the structural information offered by the OCT grayscale image.

In intravascular ultrasound (IVUS) imaging, parametric imaging techniques have been developed that quantify properties of the underlying tissue in the image. Examples of this approach are IVUS elastography, characterizing local elasticity,^{11,12,23,24} and spectral analysis methods for tissue identification.^{25–27} In intravascular OCT, published research into parametric imaging methods so far has been very limited.

Recent publications have highlighted the possibility of tissue identification in OCT images. Yabushita et al.²⁸ published a qualitative image classification scheme, which has become the *de facto* standard, distinguishing fibrous, calcified, and lipid-rich tissues. A comparison with later work by Kume et al.²⁹ reveals, however, that the interpretation of OCT images based on qualitative criteria can be ambiguous in some cases. In this study, we attempt to resolve some of the ambiguity associated with qualitative OCT tissue classification by developing a parametric imaging technique that images the optical extinction coefficient (sum of scattering and absorption: $\mu_t = \mu_s + \mu_a$) in atherosclerotic plaques *in situ*.

A few papers have been published recently^{30–32} that targeted the optical attenuation coefficient for arterial tissue identification with OCT. These studies were performed on longitudinally sectioned arteries, imaged with a scanning-stage type OCT setup. Xu et al.³³ published a study in which both the backscatter coefficient μ_b and the extinction coefficient μ_t were measured on transverse sections of paraffin-embedded, intact human coronaries. The latter study can be interpreted as a quantitative basis for the qualitative scheme of Yabushita et al.²⁸ For this work, we used an intracoronary, catheter-based OCT system, enabling us to image the optical attenuation *in situ* and even *in vivo*.

1.2 OCT Signal Model

The expectation value of the detected OCT signal $\langle I_d(r) \rangle$ can be modeled using a single scattering model that incorporates the axial point spread function due to the coupling of the

emitted and backscattered intensity to the Gaussian mode profile of a single-mode fiber³⁴ (SMF).

$$\langle I_d(r) \rangle = I_0 T(r) \hat{S}(r) \exp(-\mu_t r), \quad (1)$$

$$T(r) = \left[\left(\frac{r - z_0}{z_R} \right)^2 + 1 \right]^{-1/2}, \quad (2)$$

$$\hat{S}(r) = \begin{cases} 1 & \text{time domain OCT} \\ \exp \left[- \left(\frac{r - z_C}{z_w} \right)^2 \right] & \text{swept-source OCT.} \end{cases} \quad (3)$$

In this equation, the OCT signal is modeled by a Lambert-Beer exponential decay curve, multiplied by the coupling factor. The expectation value operator $\langle \cdot \rangle$ denotes the ensemble average over many realizations of the speckle generated by the beam in the tissue. Here $T(r)$ is the longitudinal point spread function (PSF) for an SMF-based OCT system, governed by the position of the beam waist z_0 and the Rayleigh length z_R . For analysis of Fourier-domain OCT (FD-OCT), Eq. (1) models the amplitude reflectivity.

In FD-OCT, one must also account for the spectral coherence of the source.³⁵ In this study, we use a swept-source system for *in vivo* imaging. A Gaussian coherence function $S(\nu)$ can be assumed in the frequency domain during the linear scan. The finite width of $S(\nu)$ introduces an extra factor $\hat{S}(r)$ (the Fourier transform of S), describing the signal roll-off with depth. In Eq. (3), z_C is the center of the scan, which has been moved to positive r by frequency shifting,³⁶ and z_w is the half width of the roll-off function.

Our object is the attenuation coefficient μ_t , appearing in the exponent of Eq. (1). The scale factor I_0 is the locally available intensity multiplied by the backscattering coefficient μ_b , $I_0 = \mu_b(r) I'(r)$. The backscatter efficiency is a tissue property that can be measured independently in homogeneous media.³³ The local intensity is equal to the source intensity incident on the vessel wall I_{in} diminished by the attenuation along the path from the lumen border to the imaged depth, $I'(r) = I_{in} \int_0^r \exp(-\mu_t r') dr'$. As the OCT image traces provide only one intensity measurement for every depth, it is not possible to extract two depth-dependent parameters $\mu_b(r)$ and $\mu_t(r)$ from the analysis.

Equation (1) describes the OCT signal in a homogeneous medium. The vessel wall, and biological tissue in general, are heterogeneous structures. An OCT A-line $I_d(r)$ usually samples more than one tissue type. Hence, the signal intensity must be fitted in windows of a length that is unknown *a priori*.³¹ Here, variations in $\mu_b(r)$ may confound the analysis of $\mu_t(r)$. In addition, the presence of speckle means that the signal-to-noise ratio (SNR) in the image is inherently low,^{37,38} and several frames must be averaged to reduce speckle. Averaging is complicated by artifacts due to cardiac motion, and by nonuniform catheter rotation, which can usually be corrected.^{39,40}

In this paper, we present a method for intracoronary imaging of the optical extinction coefficient μ_t . The principle is demonstrated in human coronary arteries *ex vivo*. The optical attenuation maps are compared with histopathology to iden-

tify the correspondence between tissue type and extinction coefficient. After validation, we recorded suitable intracoronary OCT sequence in patients and applied the algorithm to the data. Analysis was successful and the resulting optical attenuation maps both corroborated and complemented the qualitative interpretations of plaque type.

2 Materials and Methods

2.1 Coronary Artery Specimens

We examined 14 human coronary arteries, acquired during autopsy at the Department of Pathology of the Erasmus Medical Center (MC), from 14 human hearts (57% men, 12 left anterior descending coronary arteries, 2 right coronary arteries, mean age 64). Inclusion criteria were age >40 yr and noncardiac death. Permission to use autopsy material for scientific study was obtained from the relatives; this study was approved by the Medical Ethics Committee of the Erasmus MC.

The artery segments were excised from the heart and varied in length between 5 and 9 cm. In these vessels, 65 sites were identified (up to 5 per segment) for imaging and further histologic processing. All vessels except one were observed to be atherosclerotic based on gross pathology. During excision of the arteries, side branches were closed with sutures. OCT imaging was performed within 24 h postmortem.

2.2 Imaging Protocol In Vitro

OCT imaging was performed with an M2CV time-domain OCT system, and ImageWire 200 catheters (Lightlab Imaging Inc., Westford, Massachusetts). A vessel cross section was imaged by an IR light beam, central wavelength 1310 nm, that was swept along the vessel wall by the rotating fiber inside the catheter sheath. The OCT system had an axial resolution of 14 μm and a tangential resolution of 25 μm in the focus. The imaging depth was 3.3 mm. Each frame consisted of 312 lines \times 752 pixels, corresponding to 4.5 μm per pixel. Imaging was performed at a rate of 10 frames/ps (fps).

The artery under investigation was placed in a water bath filled with saline solution³² at 37 °C. Both ends were mounted on plastic sheaths, and the vessel was pressurized to 100 mmHg using a water column system filled with saline. The vessel was inspected longitudinally by moving the imaging catheter along the lumen. Sites of interest were marked with a needle, visible in the OCT images. At these sites, a stationary sequence of 40 to 50 frames was recorded and stored in polar coordinates in stacked TIFF (tagged image file format). After removal from the water tank, the needles were replaced by a color-coded suture.

2.3 Histopathology

After imaging, the artery sections were pressure fixed at 100 mmHg in formaldehyde for 24 h at room temperature, and subsequently stored in formaldehyde at 4 °C for further processing. Vessels were partially decalcified for 24 h in formic acid.⁴¹ After fixation and decalcification, sutures marking the imaged cross sections were replaced by ink dots. The tissue was embedded in paraffin and serially sectioned for histological staining. Each imaged cross section was stained with

Table 1 Color coding used for tissue type in the cartoon histology.

Green	Fibrous and smooth muscle cells
Yellow	Early necrotic core
Red	Advanced necrotic core
Gray	Calcification
Black	Hemorrhage

hematoxylin-eosin (H&E), picrosirius red, elastic van Gieson (EvG), and immunohistochemical stain CD68 for macrophage identification.

Histological cross sections were characterized by two pathologists blinded for the OCT results. Characterization was done by making a map of all the cross sections, called cartoon histology, with color coding for different types of tissue. We distinguished fibrous tissue, including intimal smooth muscle cells (SMCs), necrotic core in early or advanced stage, hemorrhage, and dense calcium. In case of disagreement, the two pathologists reevaluated the slides and reached a consensus diagnosis. A summary of the color coding used in the cartoon histology is given in Table 1.

2.4 Imaging Protocol In Vivo

Quantitative analysis of intracoronary OCT imagery is complicated by motion and other artifacts, resulting from catheter eccentricity or blood remnants in the lumen. The influence of cardiac motion can be mitigated by increasing the imaging speed. The diastolic filling phase, where coronary motion is minimal, lasts about 0.2 s, measured from the end of the T wave in the electrocardiogram (ECG) to the beginning of atrial systole, marked by the start of the P wave. At a frame rate of 100 fps, each heart cycle will have 15 to 20 frames in which the effects of cardiac motion are limited, and enable averaging of those frames.

In vivo imaging was performed in the catheterization laboratory of the Thorax Center of the Erasmus MC (Rotterdam, The Netherlands) using an optical frequency domain imaging (OFDI) system,^{42,43} built at the Wellman Center for Photomedicine (Boston, Massachusetts). This swept-source system had a center wavelength of 1310 nm and an axial resolution of 10 μm . The frame rate was 105 fps, and the ranging depth in tissue is about 4.7 mm. The resulting images were sampled at 512 lines \times 1024 pixels per frame.

Patients undergoing percutaneous coronary intervention (PCI) were enrolled in this study, having given informed consent. In the OFDI pullback and x-ray angiography data, lesions of interest were identified for optical attenuation imaging. The catheter imaging tip was then positioned at such a site, and a stationary (i.e., no pullback) sequence was recorded. The blood was cleared from the artery by flushing with 100% iodixanol 370 (Visipaque™, GE Healthcare, Cork, Ireland) at 37 °C, either manually or using an injection pump (Mark-V Pro Vis, Medrad Inc., Indianapolis, Pennsylvania) at 3 to 4 ml/s. Recording was started as soon as clearing was achieved, and stopped after about five heart cycles; flushing was also stopped at this time. An ECG was recorded syn-

chronously with the OCT acquisition at a sampling rate equal to the A-line frequency (54 kHz). In the acquired data, we selected the frames corresponding to the cardiac phase between the T and P waves for further analysis. The imaged plaques were classified^{2,28} by two experienced OCT readers for comparison with the assessment based on optical attenuation.

2.5 Catheter Characterization

Individual catheters of the type used in this study may have nonidentical focal length z_0 and Rayleigh length z_R . It is essential to characterize the catheters before attempting to extract quantitative data from the OCT image. Catheter beam parameters were determined by recording the OCT signal in a series of Intralipid (Fresenius Kabi, 's-Hertogenbosch, The Netherlands) dilutions (base solution 20% w/w; diluted 1:4 to 1:128) in water. Every recording consisted of about 15000 A-lines. These were averaged to reduce speckle. An r -dependent (catheter-independent) intensity offset I_{offset} was measured in water, with negligible attenuation and back-scattering. This offset was subtracted from the averaged OCT traces.

To reduce the dynamic range of the fitted signal and reduce sensitivity to noise, we linearized Eq. (1) by logarithmic compression:

$$\begin{aligned} \log[\langle I_d(r) \rangle - I_{\text{offset}}(r)] - \log[T(r; z_0, z_R)] - \log[\hat{S}(r)] \\ = \log(I_0) - \mu_t r. \end{aligned} \quad (4)$$

The second term in Eq. (4), representing the catheter-specific PSF, is calculated with Eq. (2) for a matrix of (z_0, z_R) combinations, with $0.7 \leq z_0 \leq 3$ mm and $0.2 \leq z_R \leq 1.2$ mm, both with 0.01-mm increments, and added to the offset-corrected measured intensity profile. We minimized the root mean square (rms) difference between the fitted line and measurement, compensated for roll-off if applicable, see Eq. (3). All catheters yielded a unique, paraboloid minimum. The values of z_0 and z_R at the minimum of the cost function represent the best estimate of the beam parameters.

2.6 Data Analysis

All data analysis was performed in MATLAB R2007b (The Mathworks, Natick, Massachusetts). Frames from the OCT movies were aligned using our nonlinear rotation correction algorithm,^{39,40} and then averaged for speckle reduction. This mean OCT image was used as the basis for analysis of the optical attenuation coefficients. If there was evidence of remaining motion artifacts (e.g., blurring in the averaged frame) in the corrected sequence, the data were discarded.

The intensity traces were linearized in the manner of Eq. (4), using the beam parameters specific for the catheter that was used for imaging the vessel.

$$i_d = \log[\langle I_d(r) \rangle - I_{\text{offset}}(r)] - \log[T(r)] - \log[\hat{S}(r)]. \quad (5)$$

Starting at the lumen boundary, the log-compressed data i_d was least-squares fitted with a linear model,

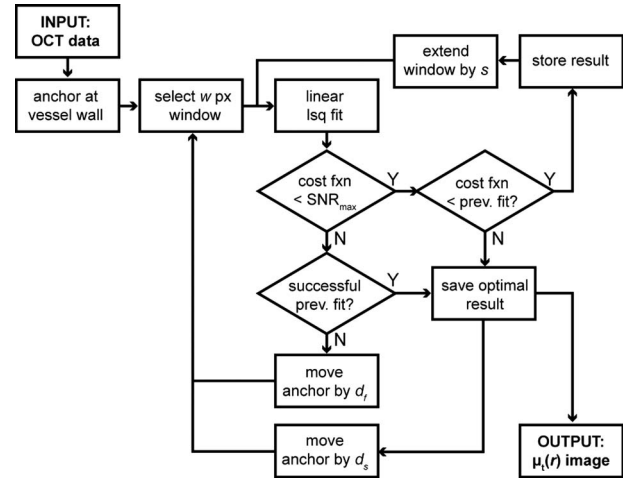


Fig. 1 Flow diagram of the fitting process. Several intermediate steps enable the algorithm to handle discontinuities and noise. Full description in the text.

$$\tilde{i}(r) = \log(I_0) - \mu_t r, \quad (6)$$

in a window of variable length L . With a linear optimization, there is a unique optimum for each set of data, and results are independent of the initial guess required for an iterative non-linear model. Speed is another advantage.

We extracted μ_t from the data, using a fitting procedure optimized to search for homogeneous tissue regions. The fitting window was extended until an inhomogeneity was encountered that degraded the result. Searching for the longest window maximizes the accuracy of the fitted attenuation coefficient, and reduces sensitivity to intensity fluctuations that result from μ_b inhomogeneities.

A schematic representing the data flow in the fitting procedure is shown in Fig. 1. Using an adaptive threshold criterion, the lumen boundary is determined in the mean image. A linear least-squares (lsq) fit is performed in a window of minimum length $L_{\text{min}} = 200 \mu\text{m}$, corresponding to $w = 44$ pixels (px). Results with $\mu_t < 0$ are discarded. The cost function (fxn) δ is defined as the root of mean square (rms) difference between the measured OCT trace i_d [Eq. (5)] and the model \tilde{i} . The window is iteratively extended until a decrease in fit quality is detected. The optimum values (for smallest δ) are stored, and the window is moved forward. This procedure is repeated until the window encounters the end of the A-line. All parameters in the fitting procedure were optimized in a simulation study.⁴⁴

This algorithm results in an estimate of $\mu_t(r)$ for every A-line. The attenuation coefficients are color coded on a linear scale and plotted in the regular gray-scale OCT image as an overlay or side by side. The *in vitro* attenuation image is then compared with the cartoon histology to identify a correspondence between tissue type and μ_t . As histological tissue slices are much thinner ($5 \mu\text{m}$) than the accuracy of the needle marker (≈ 0.5 mm) there is an unavoidable sampling error.^{45–47} Imaged cross sections that were obviously mismatched with histology, based on anatomical features, were removed from the data set before analysis.

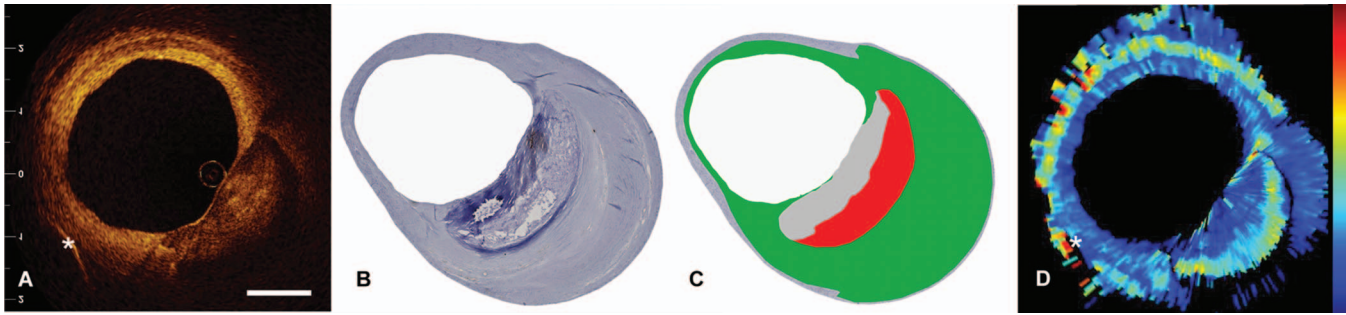


Fig. 2 (A) OCT image of a coronary atherosclerotic lesion *ex vivo*: * indicates the needle used for marking the imaged site, the length of the white scale bar is 1 mm; (B) corresponding histology, H&E stain; (C) cartoon histology, overlaid on the original histology slide, indicating an advanced necrotic core (red) behind a calcification (gray), and a slight fibrotic (green) circumferential intimal thickening; and (D) OCT-derived attenuation coefficient μ_v , plotted on a continuous linear color scale from 0 to 15 mm^{-1} . The area corresponding to the necrotic core exhibits a higher attenuation coefficient (8 to 10 mm^{-1}) than the calcification next to it or the surrounding fibrous tissue (2 to 3 mm^{-1}).

3 Results

3.1 In Vitro Imaging

We analyzed OCT data of 39 lesions. Other sites had either too much catheter motion, preventing the averaging of the data, or the match between the OCT data and histology was inaccurate. Results for different lesion types are shown in Figs. 2–4. Figure 2 displays data for a lesion containing a large calcification and an advanced necrotic core. Low attenuation is found in areas with fibrous tissue and calcification. The necrotic core exhibits a high attenuation coefficient, and stands out much more clearly in the attenuation image than in the gray-scale OCT. The adventitia also has a high attenuation, but can be distinguished from pathological features by its morphology and location: the high attenuation region occurs outside the media and is circumferential. A concentric fibrous lesion shows up as a homogenous, circumferential, low-attenuation region in Fig. 3. Again, the attenuation coefficient rises in the adventitial region.

A more complex plaque type is analyzed in Fig. 4. The OCT image is very heterogeneous, and this is reflected by the morphology in the histology. The cartoon histology shows intraplaque hemorrhage and necrotic core, embedded in a mostly fibrous matrix. The green and orange boxes highlight areas with high attenuation coefficient. The green box contains some necrotic core, which is in accordance with the example in Fig. 2. The orange box, however, is only fibrous tissue and SMC. The CD68 stain reveals strong topical macrophage infiltration in both these areas. Macrophages, being strong optical scatterers, attenuate the OCT beam. An example of intimal xanthoma is shown in Fig. 5. Macrophages in a lesion that is mostly fibrous otherwise cause strong attenuation.

The limited size and composition of our data set does not permit formulation of a statistically sound, quantitative classification scheme for automatic identification of necrotic core and macrophages, or plaque type in general. We can, however, formulate tentative criteria based on the appearance of certain pathologies in our *in vitro* optical attenuation data. The characteristics we observed are summarized in Table 2.

3.2 In Vivo Imaging

Stationary OCT sequences with ECG registration were obtained from nine sites in four patients. Of these, eight sites had OFDI data with small enough catheter motion that the residual shifts could be corrected and the frames could be averaged in at least one heart cycle. Of the imaged plaques, five were classified as fibroatheroma, and three were fibrous lesions. Figure 6 presents optical attenuation imaging of atherosclerotic lesions *in vivo* in two plaques of different types.

The measured optical attenuation reproduces accurately if a single site is imaged repeatedly. In Fig. 7, we show attenuation data from a necrotic-core coronary lesion *in vivo*, imaged over three consecutive heart cycles. The features observed in the plaque, as well as the absolute values of the

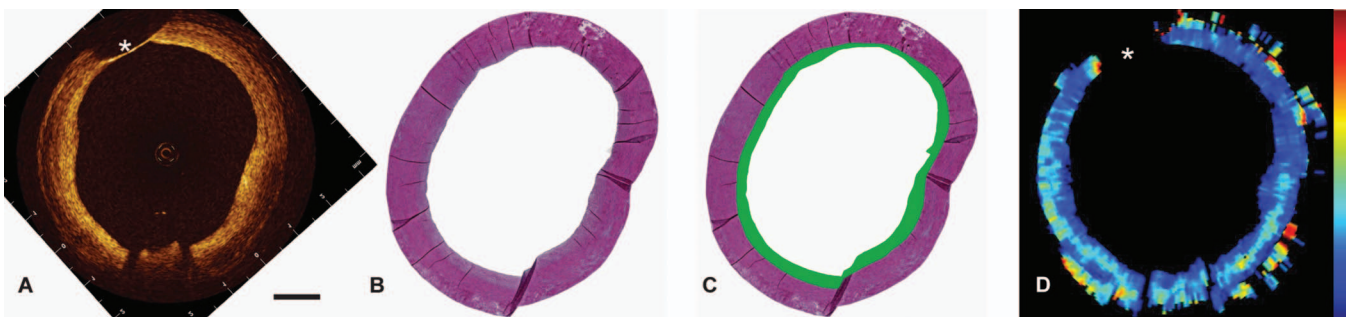


Fig. 3 (A) OCT image of a circumferential homogeneous intimal thickening case, length of the scale bar is 1 mm; (B) corresponding histology, EvG stain; (C) cartoon histology, highlighting a fibrous thickened intima; and (D) the attenuation coefficient μ_t is uniform and low, 2 to 4 mm^{-1} , in the area corresponding to the fibrous lesion. The color scale runs from 0 to 15 mm^{-1} .

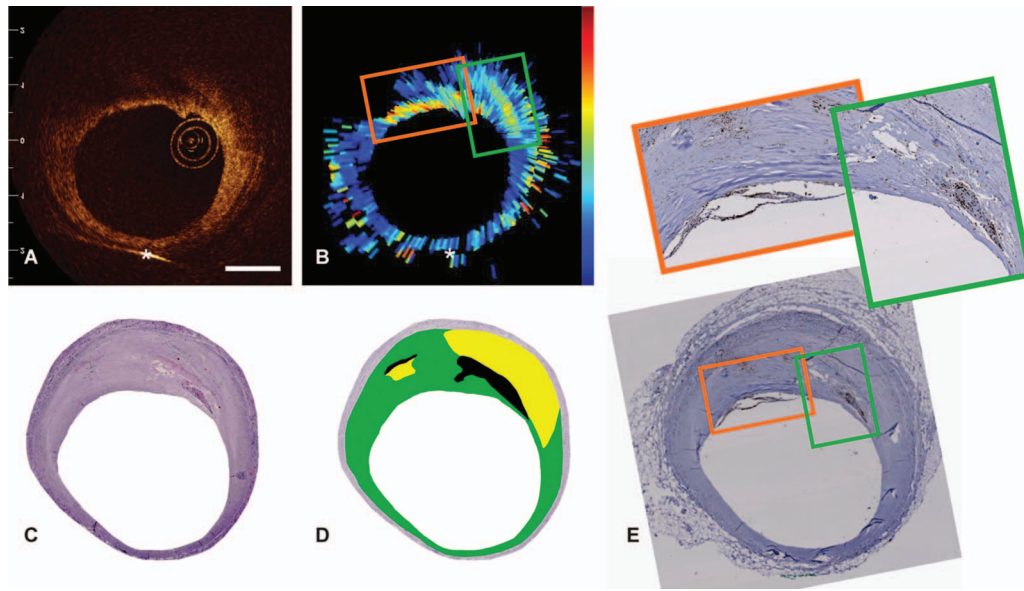


Fig. 4 Complex lesion containing necrotic core, hemorrhage, and macrophages: (A) OCT image, scale bar corresponds to 1 mm; (B) attenuation coefficient, scale from 0 to 15 mm⁻¹; (C) histology, H&E stain; (D) cartoon indicating an early stage necrotic lesion (yellow) with a thin fibrous cap and intraplaque hemorrhage (black); and (E) CD68 stain, showing macrophage infiltration. The green and orange boxes are magnified (2.25× with respect to the overview) above, and correspond to the indicated areas in (B). Both areas show high attenuation coefficients (10 to 12 mm⁻¹), coinciding with the presence of necrotic core (green box) and macrophages (green and orange boxes).

attenuation coefficient, appear very similar in the different images. A quantitative estimate of the reproducibility is not straightforward as the data from different heart cycles are not exactly aligned angularly and radially.

The characteristics noted in Table 2 were also observed *in vivo*, as evidenced by Fig. 6. Plaque identification by application of these criteria agreed with the interpretation by two OCT readers for seven out of eight cases. Interpretation of the last one (a fibrous plaque by gray scale; significant necrotic core according to optical attenuation) was complicated by inhomogeneity in both the gray-scale and attenuation images.

4 Discussion

4.1 Study Results

We compared the optical attenuation coefficient, measured by OCT, with the composition of atherosclerotic lesions, based on histology. High optical attenuation— $\mu_t \geq 10 \text{ mm}^{-1}$ —is associated with two important markers of atherosclerotic plaque vulnerability: necrotic core and macrophage infiltration. Other

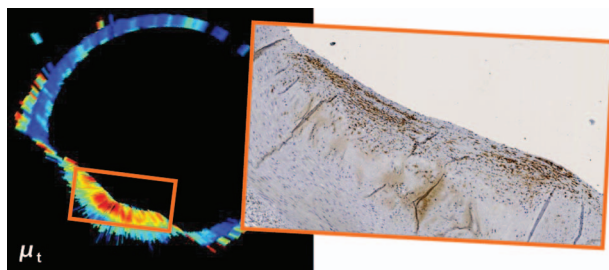


Fig. 5 Intimal xanthoma case. High attenuation (color scale 0 to 15 mm⁻¹ as before) in a fibrous lesion occurs due to macrophage infiltration, as evidenced by the CD68 stain in the inset.

common plaque tissue types, fibrous and calcific, were found to have a low attenuation coefficient— $\mu_t \approx 2 \text{ to } 4 \text{ mm}^{-1}$. The *in vitro* measurements were done on intact excised human coronary arteries, with a commercially available, clinically approved OCT system and catheters.

We demonstrated that the analysis can be performed, with similar results, on patient data. The application in interventional procedures is easy, quick, and does not cause any patient discomfort. It requires the recording of a stationary se-

Table 2 Appearance of vessel wall condition in the attenuation image.

Condition	Appearance	Typical μ_t
Healthy vessel wall	Thin (<300 μm) circumferential layer of low attenuation, adjacent to the lumen;	2 to 5 mm ⁻¹
	enveloped by a circumferential high-attenuation layer	>12 mm ⁻¹
Intimal thickening	Circumferential layer of low attenuation adjacent to the lumen; thickness $\geq 500 \mu\text{m}$	2 to 5 mm ⁻¹
Necrotic core	Asymmetric area of high attenuation	$\approx 10 \text{ mm}^{-1}$
Macrophage infiltration	Layer of high attenuation, possibly missing data behind it	>12 mm ⁻¹

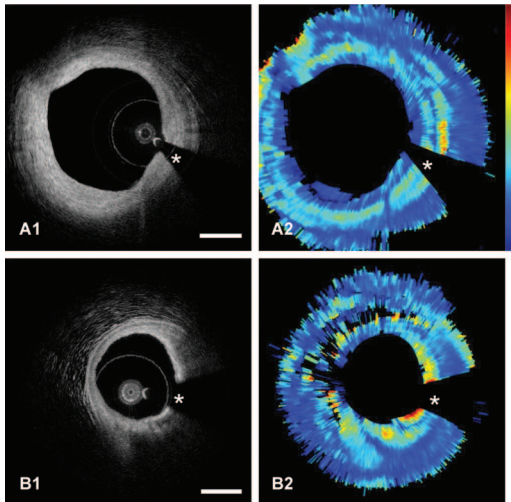


Fig. 6 Optical attenuation imaging *in vivo*. Left column: OFDI images; right column: optical attenuation; * marks the guidewire shadow. The length of the white scale bars is 1 mm. The color scale runs from 0 to 15 mm^{-1} . (A) A case of circumferential pathological intimal thickening. The fibrous tissue in the plaque is evident from its bright signal (A1) and low attenuation coefficient (A2). (B) Another example of a lipid-rich plaque (2 to 5 o'clock), with possible macrophage infiltration in the cap (below the guidewire shadow; B1). The attenuation coefficient (B2) is high ($\mu_t \approx 10 \text{ mm}^{-1}$) throughout the plaque, with values up to 15 mm^{-1} in the macrophage area.

quence of about five heart cycles at a spot of interest, and about 25 ml of extra flush medium for clearing.

Automated, intraprocedural, real-time attenuation analysis should be possible, if the OCT catheters are well-characterized before imaging. The only steps that currently require user attention are the selection of end-diastolic frames for processing, and a check to ensure the lumen contour detection did not produce any errors. Data processing is computationally light: analysis of a cross section takes 1 to 2 s (de-

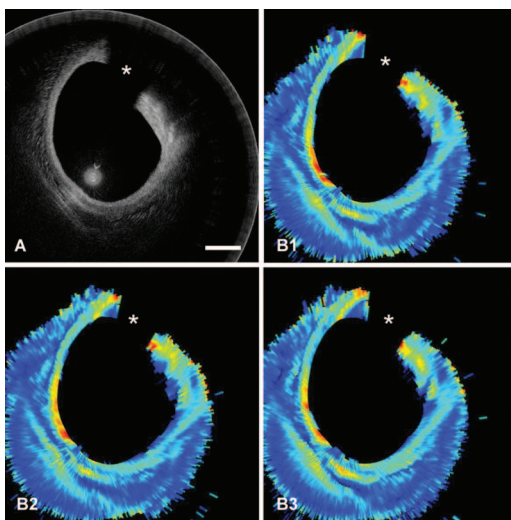


Fig. 7 (A) Coronary lesion, imaged with OFDI *in vivo*; (B1) to (B3) Optical attenuation coefficient from the cross section in three consecutive heart cycles, demonstrating the reproducibility of the algorithm. The data in (B1) correspond to the gray-scale image in (A).

pending on frame size) in MATLAB on an office PC, without any custom optimization.

This study is the first to report *in situ* tissue typing of atherosclerotic lesions in intact human coronary arteries by means of the optical attenuation coefficient. It is also the first to demonstrate the *in vivo* feasibility of such an approach, and to assess the diagnostic potential of this parameter for plaque type in a clinical setting. One of the main difficulties in OCT-based plaque characterization is the distinction between necrotic core and calcified lesions, as the difference is only in border definition.^{28,29} In optical attenuation, there is a marked contrast between the two plaque components.

The analyzed attenuation coefficients for the different tissue types are similar *in vivo* compared to *in vitro*. Given that the two data sets were acquired with fundamentally different OCT systems, and different catheters, this inspires confidence in the data. It also suggests that the tissue optical properties did not change significantly after excision of the arteries at autopsy and storage in saline during the experiment.

4.2 Comparison with Literature

Our results are in general agreement with those presented by Xu et al.³³ Using a benchtop OCT system, they measured low μ_t for fibrous and calcific tissue and high μ_t for necrotic core. Macrophage infiltration was not identified in that study. The scale is also comparable, taking uncertainty margins into account and reading the “lipid” category of Ref. 33 as our category “necrotic:” necrotic core has $\mu_t > 10 \text{ mm}^{-1}$. Xu et al. report a value of the fibrous and calcific, $\mu_t \approx 6 \text{ mm}^{-1}$, that is slightly larger than the one we found ($\mu_t \approx 2$ to 5 mm^{-1}). This may be a result of the fixation procedure applied in Ref. 33.

Other literature reports both higher³⁰ and lower³¹ values for necrotic core attenuation. Our data do confirm the observation³³ that lipid-rich tissue attenuates more strongly than other atherosclerotic tissue types, or healthy vascular tissue.

4.3 Image Artifacts and Study Limitations

We were unable to determine the backscatter coefficient μ_b from our data because of tissue heterogeneity and the lack of an intensity calibration (I_{in} in Sec. 1.2) that is constant for all lines and frames. We put in a significant effort to reduce the sensitivity of the fitting algorithm to sudden steps in intensity that result from a drop in μ_b at a sharp interface between different tissues. This approach has been successful, by and large, but evidence of artifacts, resulting from changes in μ_b being interpreted as large μ_t , remains in the data. An example can be seen in Fig. 2, where fibrous and calcified tissue are adjacent. Both fibrous and calcified tissue have a low μ_t , but the transition from high μ_b (fibrous) to low μ_b (calcified) produces a spot of high fitted μ_t near 3 o'clock. This illustrates that the attenuation display should always be interpreted in conjunction with the gray-scale OCT image.

The model we used for analysis is a single-scattering model, assuming straight light paths to and from the scattering site where backreflection occurs, and not incorporating interfaces between different tissues. In reality, specular interface reflections at the boundary between different tissues—with differing refractive indices³²—may produce a strong signal

locally, which cannot be accounted for by Eq. (1). Likewise, there is evidence of multiple scattering, causing a higher signal than predicted by the model, depending on beam parameters and tissue optical properties.^{48,49} More sophisticated optical modeling⁵⁰ could reduce these artifacts, but will substantially complicate the analysis and increase dependence on parameter guesses.

Two aspects of the comparison with histology merit discussion. The first is in-plane (as opposed to longitudinal, pointed out in Sec. 2.6) image registration: the histologic processing inevitably deforms the tissue. This complicates automated correlation and one-to-one mapping between tissue type and optical attenuation.

Second, density variations are apparent in the histology slides, particularly in fibrous tissue. Certain areas seem to be more tightly packed than others. While in some cases this may be an artifact due to histologic processing, these regions can often be identified in the OCT images as well, thus representing real tissue inhomogeneities. They will undoubtedly reflect in the attenuation coefficient. Our standard—tissue type, color coded in the cartoon histology—does not represent these density variations. This is a source of μ_t variation that our analysis cannot account for. Likewise, for the *in vivo* data, the plaque classification is more coarse-grained than our image analysis. It qualifies an entire cross section as a certain plaque type and cannot account for possible variability within a plaque that will be apparent in our data.

Routine clinical use of the tissue characterization method is limited in its present implementation by the frame averaging used for speckle reduction. Multiple frame processing is incompatible with imaging of a coronary artery in a pullback, where each frame samples a different vascular cross section. The required amount of speckle reduction depends on the minimum acceptable SNR for the fit results to be meaningful. An unpolarized OCT image theoretically has³⁷ $\text{SNR} = \langle I \rangle / \sigma_I = 1.4$; we observe $\text{SNR} = 1.8$ to 2.0 in our *in vitro* data and $\text{SNR} = 1.7$ to 1.9 *in vivo*. Averaging N independent speckles increases the SNR as \sqrt{N} . We found heuristically that, with the present algorithm, about 30 frames are required in the *in vitro* data, while 15 to 20 frames suffice *in vivo*. The difference may be attributed to residual cardiac motion, assisting speckle decorrelation between frames. In the future, we will investigate more sophisticated speckle reduction and data processing techniques, such as frequency compounding in FD-OCT data or digital filtering,⁵¹⁻⁵³ to enable comprehensive imaging of the optical attenuation in a coronary artery.

5 Conclusions

We developed a framework for imaging the optical attenuation coefficient μ_t in human coronary arteries using intravascular OCT. *In vitro* studies demonstrate that μ_t is a suitable parameter to distinguish between different tissue types in atherosclerotic lesions. Two markers of plaque vulnerability, the presence of necrotic core and macrophage infiltration, can be identified as areas of high attenuation ($\mu_t \geq 10 \text{ mm}^{-1}$). Fibrous and calcified tissue have $\mu_t \approx 2-5 \text{ mm}^{-1}$. The analysis was successfully applied to OCT images acquired in patients. Optical-attenuation-based plaque classification, using the criteria developed with the *in vitro* analysis, corroborated the plaque classification based on the gray-scale OCT.

References

1. E. Falk, P. K. Shah, and V. Fuster, "Coronary plaque disruption," *Circulation* **92**(3), 657–671 (1995).
2. R. Virmani, F. D. Kolodgie, A. P. Burke, A. Farb, and S. M. Schwartz, "Lessons from sudden coronary death—a comprehensive morphological classification scheme for atherosclerotic lesions," *Arterioscler., Thromb., Vasc. Biol.* **20**(5), 1262–1275 (2000).
3. E. Falk, "Plaque rupture with severe pre-existing stenosis precipitating coronary thrombosis: characteristics of coronary atherosclerotic plaques underlying fatal occlusive thrombi," *Br. Heart J.* **50**(2), 127–134 (1983).
4. F. D. Kolodgie, A. P. Burke, A. Farb, H. K. Gold, J. Y. Yuan, J. Narula, A. V. Finn, and R. Virmani, "The thin-cap fibroatheroma, a type of vulnerable plaque—the major precursor lesion to acute coronary syndromes," *Curr. Opin. Cardiol.* **16**(5), 285–292 (2001).
5. J. A. Schaar, J. E. Muller, E. Falk, R. Virmani, V. Fuster, P. W. Serruys, A. Colombo, C. Stefanadis, W. S. Casscells, P. R. Moreno, A. Maseri, and A. F. W. van der Steen, "Terminology for high-risk and vulnerable coronary artery plaques," *Eur. Heart J.* **25**(12), 1077–1082 (2004).
6. P. W. Serruys, H. M. Garcia-Garcia, and E. Regar, "From postmortem characterization to the *in vivo* detection of thin-capped fibroatheromas: the missing link toward percutaneous treatment: what if Diogenes would have found what he was looking for?" *J. Am. Coll. Cardiol.* **50**(10), 950–952 (2007).
7. S. Waxman, F. Ishibashi, and J. E. Muller, "Detection and treatment of vulnerable plaques and vulnerable patients—novel approaches to prevention of coronary events," *Circulation* **114**(22), 2390–2411 (2006).
8. P. D. Richardson, M. J. Davies, and G. V. Born, "Influence of plaque configuration and stress distribution on fissuring of coronary atherosclerotic plaques," *Lancet* **334**(8669), 941–944 (1989).
9. R. Virmani, F. D. Kolodgie, A. P. Burke, A. V. Finn, H. K. Gold, T. N. Tulenko, S. P. Wrenn, and J. Narula, "Atherosclerotic plaque progression and vulnerability to rupture—angiogenesis as a source of intraplaque hemorrhage," *Arterioscler., Thromb., Vasc. Biol.* **25**(10), 2054–2061 (2005).
10. E. Falk, "Pathogenesis of atherosclerosis," *J. Am. Coll. Cardiol.* **47**(8), C7–C12 (2006).
11. J. A. Schaar, C. L. de Korte, F. Mastik, C. Strijder, G. Pasterkamp, E. Boersma, P. W. Serruys, and A. F. W. van der Steen, "Characterizing vulnerable plaque features with intravascular elastography," *Circulation* **108**(21), 2636–2641 (2003).
12. C. L. de Korte, M. J. Siervogel, F. Mastik, C. Strijder, J. A. Schaar, E. Velema, G. Pasterkamp, P. W. Serruys, and A. F. W. van der Steen, "Identification of atherosclerotic plaque components with intravascular ultrasound elastography *in vivo*: a Yucatan pig study," *Circulation* **105**(14), 1627–1630 (2002).
13. D. E. Goertz, M. E. Frijlink, D. Tempel, V. Bhagwandas, A. Gisolf, R. Krams, N. de Jong, and A. F. W. van der Steen, "Subharmonic contrast intravascular ultrasound for vasa vasorum imaging," *Ultrasound Med. Biol.* **33**(12), 1859–1872 (2007).
14. D. E. Goertz, M. E. Frijlink, D. Tempel, L. C. A. van Damme, R. Krams, J. A. Schaar, F. J. ten Cate, P. W. Serruys, N. de Jong, and A. F. W. van der Steen, "Contrast harmonic intravascular ultrasound—a feasibility study for vasa vasorum imaging," *Invest. Radiol.* **41**(8), 631–638 (2006).
15. P. R. Moreno, R. A. Lodder, K. R. Purushothaman, W. E. Charash, W. N. O'Connor, and J. E. Muller, "Detection of lipid pool, thin fibrous cap, and inflammatory cells in human aortic atherosclerotic plaques by near-infrared spectroscopy," *Circulation* **105**(8), 923–927 (2002).
16. B. D. MacNeill, I. K. Jang, B. E. Bouma, N. Iftimia, M. Takano, H. Yabushita, M. Shishkov, C. R. Kaufman, S. L. Houser, H. T. Aretz, D. DeJoseph, E. F. Halpern, and G. J. Tearney, "Focal and multi-focal plaque distributions in patients with macrophage acute and stable presentations of coronary artery disease," *J. Am. Coll. Cardiol.* **44**(5), 972–979 (2004).
17. M. Takano, I. K. Jang, S. Inami, M. Yamamoto, D. Murakami, K. Okamoto, K. Seimiya, T. Ohba, and K. Mizuno, "*In vivo* comparison of optical coherence tomography and angiography for the evaluation of coronary plaque characteristics," *Am. J. Cardiol.* **101**(4), 471–476 (2008).
18. O. C. Raffel, F. M. Merchant, G. J. Tearney, S. Chia, D. D. Gauthier, E. Pomerantsev, K. Mizuno, B. E. Bouma, and I.-K. Jang, "*In vivo* association between positive coronary artery remodelling and coro-

- nary plaque characteristics assessed by intravascular optical coherence tomography," *Eur. Heart J.* **29**(14), 1721–1728 (2008).
19. P. Barlis, P. W. Serruys, N. Gonzalo, W. J. van der Giessen, P. J. de Jaegere, and E. Regar, "Assessment of culprit and remote coronary narrowings using optical coherence tomography with long-term outcomes," *Am. J. Cardiol.* **102**(4): 391–395 (2008).
 20. T. Kubo, T. Imanishi, H. Kitabata, A. Kuroi, S. Ueno, T. Yamano, T. Tanimoto, Y. Matsuo, T. Masho, S. Takarada, A. Tanaka, N. Nakamura, M. Mizukoshi, Y. Tomobuchi, and T. Akasaka, "Comparison of vascular response after sirolimus-eluting stent implantation between patients with unstable and stable angina pectoris, a serial optical coherence tomography study," *J. Am. Coll. Cardiol. Imaging* **1**(4), 475–484 (2008).
 21. R. Virmani, A. P. Burke, A. Farb, and F. D. Kolodgie, "Pathology of the vulnerable plaque," *J. Am. Coll. Cardiol.* **47**(8), C13–C18 (2006).
 22. T. Kubo, T. Imanishi, S. Takarada, A. Kuroi, S. Ueno, T. Yamano, T. Tanimoto, Y. Matsuo, T. Masho, H. Kitabata, K. Tsuda, Y. Tomobuchi, and T. Akasaka, "Assessment of culprit lesion morphology in acute myocardial infarction—ability of optical coherence tomography compared with intravascular ultrasound and coronary angiography," *J. Am. Coll. Cardiol.* **50**(10), 933–939 (2007).
 23. B. M. Shapo, J. R. Crowe, A. R. Skovoroda, M. J. Eberle, N. A. Cohn, and M. O'Donnell, "Displacement and strain imaging of coronary arteries with intraluminal ultrasound," *IEEE Trans. Ultrason. Ferroelectr. Freq. Control* **43**(2), 234–246 (1996).
 24. E. I. Cespedes, C. L. de Korte, and A. F. W. van der Steen, "Intraluminal ultrasonic palpation, assessment of local and cross-sectional tissue stiffness," *Ultrasound Med. Biol.* **26**(3), 385–396 (2000).
 25. A. Nair, B. D. Kuban, N. Obuchowski, and D. G. Vince, "Assessing spectral algorithms to predict atherosclerotic plaque composition with normalized and raw intravascular ultrasound data," *Ultrasound Med. Biol.* **27**(10), 1319–1331 (2001).
 26. A. Nair, B. D. Kuban, E. M. Tuzcu, P. Schoenhagen, S. E. Nissen, and D. G. Vince, "Coronary plaque classification with intravascular ultrasound radiofrequency data analysis," *Circulation* **106**(17), 2200–2206 (2002).
 27. A. Katouzian, S. Sathyanarayana, B. Baseri, E. E. Konofagou, and S. G. Carlier, "Challenges in atherosclerotic plaque characterization with intravascular ultrasound (IVUS): from data collection to classification," *IEEE Trans. Inf. Technol. Biomed.* **12**(3), 315–327 (2008).
 28. H. Yabushita, B. E. Bouma, S. L. Houser, T. Aretz, I. K. Jang, K. H. Schlendorf, C. R. Kauffman, M. Shishkov, D. H. Kang, E. F. Halpern, and G. J. Tearney, "Characterization of human atherosclerosis by optical coherence tomography," *Circulation* **106**(13), 1640–1645 (2002).
 29. T. Kume, T. Akasaka, T. Kawamoto, N. Watanabe, E. Toyota, Y. Neishi, R. Sukmawan, Y. Sadahira, and K. Yoshida, "Assessment of coronary arterial plaque by optical coherence tomography," *Am. J. Cardiol.* **97**(8), 1172–5 (2006).
 30. D. Levitz, L. Thrane, M. Frosz, P. Andersen, C. Andersen, J. Valancianaite, J. Swartling, S. Andersson-Engels, and P. Hansen, "Determination of optical scattering properties of highly-scattering media in optical coherence tomography images," *Opt. Express* **12**(2), 249–259 (2004).
 31. F. J. van der Meer, D. J. Faber, D. M. Baraznji Sassoon, M. C. Aalders, G. Pasterkamp, and T. G. van Leeuwen, "Localized measurement of optical attenuation coefficients of atherosclerotic plaque constituents by quantitative optical coherence tomography," *IEEE Trans. Med. Imaging* **24**(10), 1369–76 (2005).
 32. F. J. van der Meer, D. J. Faber, I. Cilesiz, M. J. C. van Gemert, and T. G. van Leeuwen, "Temperature-dependent optical properties of individual vascular wall components measured by optical coherence tomography," *J. Biomed. Opt.* **11**(4), 041120 (2006).
 33. C. Xu, J. M. Schmitt, S. G. Carlier, and R. Virmani, "Characterization of atherosclerosis plaques by measuring both backscattering and attenuation coefficients in optical coherence tomography," *J. Biomed. Opt.* **13**(3), 034003 (2008).
 34. T. G. van Leeuwen, D. J. Faber, and M. C. Aalders, "Measurement of the axial point spread function in scattering media using single-mode fiber-based optical coherence tomography," *IEEE J. Sel. Top. Quantum Electron.* **9**(2), 227–233 (2003).
 35. R. Leitgeb, C. K. Hitzenberger, and A. F. Fercher, "Performance of Fourier domain vs. time domain optical coherence tomography," *Opt. Express* **11**(8), 889–894 (2003).
 36. S. H. Yun, G. J. Tearney, J. F. de Boer, and B. E. Bouma, "Removing the depth-degeneracy in optical frequency domain imaging with frequency shifting," *Opt. Express* **12**(20), 4822–4828 (2004).
 37. J. M. Schmitt, S. H. Xiang, and K. M. Yung, "Speckle in optical coherence tomography," *J. Biomed. Opt.* **4**(1), 95–105 (1999).
 38. J. Rogowska and M. E. Brezinski, "Evaluation of the adaptive speckle suppression filter for coronary optical coherence tomography imaging," *IEEE Trans. Med. Imaging* **19**(12), 1261–1266 (2000).
 39. G. van Soest, J. G. Bosch, and A. F. W. van der Steen, "Azimuthal registration of image sequences affected by nonuniform rotation distortion," *IEEE Trans. Inf. Technol. Biomed.* **12**(3), 348–355 (2008).
 40. G. van Soest, J. G. Bosch, and A. F. W. van der Steen, "Alignment of intravascular optical coherence tomography movies affected by non-uniform rotation distortion," *Proc. SPIE* **6847**, 684721–8 (2008).
 41. G. J. Friedrich, N. Y. Moes, V. A. Muhlberger, C. Gabl, G. Mikuz, D. Hausmann, P. J. Fitzgerald, and P. G. Yock, "Detection of intralésional calcium by intracoronary ultrasound depends on the histologic pattern," *Am. Heart J.* **128**(3), 435–441 (1994).
 42. S. H. Yun, G. J. Tearney, B. J. Vakoc, M. Shishkov, W. Y. Oh, A. E. Desjardins, M. J. Suter, R. C. Chan, J. A. Evans, I.-K. Jang, N. S. Nishioka, J. F. de Boer, and B. E. Bouma, "Comprehensive volumetric optical microscopy *in vivo*," *Nat. Med.* **12**(12), 1429–1433 (2007).
 43. G. J. Tearney, S. Waxman, M. Shishkov, B. J. Vakoc, M. J. Suter, M. I. Freilich, A. E. Desjardins, W.-Y. Oh, L. A. Bartlett, M. Rosenberg, and B. E. Bouma, "Three-dimensional coronary artery microscopy by intracoronary optical frequency domain imaging," *J. Am. Coll. Cardiol. Imaging* **1**(6), 752–761 (2008).
 44. G. van Soest, T. P. M. Goderie, S. van Noorden, and A. F. W. van der Steen, "Algorithm optimization for quantitative analysis of intravascular optical coherence tomography data," *Proc. SPIE* **7161**, 71612C-8 (2009).
 45. J. Rieber, O. Meissner, G. Babaryka, S. Reim, M. Oswald, A. Koenig, T. M. Schiele, M. Shapiro, K. Theisen, M. F. Reiser, V. Klaus, and U. Hoffmann, "Diagnostic accuracy of optical coherence tomography and intravascular ultrasound for the detection and characterization of atherosclerotic plaque composition in ex-vivo coronary specimens: a comparison with histology," *Coron Artery Dis.* **17**(5), 425–430 (2006).
 46. O. A. Meissner, J. Rieber, G. Babaryka, M. Oswald, S. Reim, U. Siebert, T. Redel, M. Reiser, and U. Mueller-Lisse, "Intravascular optical coherence tomography, comparison with histopathology in atherosclerotic peripheral artery specimens," *J. Vasc. Interv. Radiol.* **17**(2), 343–349 (2006).
 47. N. Bruining, S. Verheye, M. Knaapen, P. Somers, J. Roelandt, E. Regar, I. Heller, S. de Winter, J. Ligthart, G. Van Langenhove, P. J. de Feyter, P. W. Serruys, and R. Hamers, "Three-dimensional and quantitative analysis of atherosclerotic plaque composition by automated differential echogenicity," *Catheter. Cardiovasc. Interv.* **70**(7), 968–978 (2007).
 48. J. M. Schmitt, A. Knüttel, M. J. Yadlowsky, and M. A. Eckhaus, "Optical-coherence tomography of a dense tissue—statistics of attenuation and backscattering," *Phys. Med. Biol.* **39**(10), 1705–1720 (1994).
 49. M. J. Yadlowsky, J. M. Schmitt, and R. F. Bonner, "Multiple scattering in optical coherence tomography," *Appl. Opt.* **34**(25), 5699–5707 (1995).
 50. L. Thrane, M. H. Frosz, T. M. Jørgensen, A. Tycho, H. T. Yura, and P. E. Andersen, "Extraction of optical scattering parameters and attenuation compensation in optical coherence tomography images of multilayered tissue structures," *Opt. Lett.* **29**(14), 1641–1643 (2004).
 51. M. Bircher, E. Gotzinger, R. Leitgeb, A. F. Fercher, and C. K. Hitzenberger, "Speckle reduction in optical coherence tomography by frequency compounding," *J. Biomed. Opt.* **8**(3), 565–569 (2003).
 52. D. C. Adler, T. H. Ko, and J. G. Fujimoto, "Speckle reduction in optical coherence tomography images by use of a spatially adaptive wavelet filter," *Opt. Lett.* **29**(24), 2878–2880 (2004).
 53. A. Ozcan, A. Bilenca, A. E. Desjardins, B. E. Bouma, and G. J. Tearney, "Speckle reduction in optical coherence tomography images using digital filtering," *J. Opt. Soc. Am. A* **24**(7), 1901–1910 (2007).